

Optics Letters

Theoretical analysis of ultrahigh figure of merit sensing in plasmonic waveguides with a multimode stub

ZHIHUI HE,¹ HONGJIAN LI,^{1,2,*} BOXUN LI,¹ ZHIQUAN CHEN,¹ HUI XU,¹ AND MINGFEI ZHENG¹

¹College of Physics and Electronics, Central South University, Changsha 410083, China

²College of Materials Science and Engineering, Central South University, Changsha 410083, China

*Corresponding author: lihj398@126.com

Received 24 August 2016; revised 8 October 2016; accepted 12 October 2016; posted 13 October 2016 (Doc. ID 274457); published 7 November 2016

We propose an expanded coupled mode theory to analyze sensing performance in a plasmonic slot waveguide side-coupled with a multimode stub resonator. It is confirmed by the finite-difference time-domain simulations. Through adjusting the parameters, we can realize figure of merit (FOM) of $\sim 59,010$, and the sensitivity S can reach to 75.7. Compared with the plasmonic waveguide systems in recent Letters, our proposed structure has the advantages of easy fabrication, compactness, sensitivity, and high FOM. The proposed theory model and findings provide guidance for fundamental research of the integrated plasmonic nano-sensor applications. © 2016 Optical Society of America

OCIS codes: (240.6680) Surface plasmons; (230.7370) Waveguides; (130.3120) Integrated optics devices.

<http://dx.doi.org/10.1364/OL.41.005206>

Surface plasmon polaritons (SPPs), which can manipulate light on a nanoscale structure beyond the diffraction limit [1–3], provide opportunities for many fascinating researches like optical filters [4,5], biomedicine, [6] and switching [7–9]. SPPs exhibit special responses such as the high confinement and localized enhancement of field, which can be used to improve the absorption of active materials [10,11]. Nanoplasmonic waveguides, supporting the propagation of SPPs and manipulating light on a subwavelength scale, can be regarded as an ideal optical element in an integrated plasmonic device [12,13]. Among a variety of plasmonic waveguide structures, metal–dielectric–metal (MDM) waveguides are of particular interest because they are easily fabricated and have deep subwavelength confinement of light with an acceptable propagation length for SPPs [14–19]. Recently, the MDM waveguide structure, with advantages of easy fabrication and convenient integration and light manipulation, has also become available for sensor research [20–24]. Zhan *et al.* reported a plasmonic bright–dark mode waveguide system and achieved figure of merit (FOM) over 20,000 [20]. Huang *et al.* reported that slow light can enhance the sensitivity in plasmonic waveguide

sensors [21]. In our recent work, we introduced radiation-oscillator theory to investigate spectral responses and sensing applications in a plasmonic waveguide with multimode stub [22]. However, we did not discuss the sensing performance as a function of parameters in the slot waveguide side-coupled with a multimode stub. In addition, a proper theoretical model, which can be used to predict the sensing performance of structures, was established in recent Letters.

In this Letter, we introduce an expanded coupled mode theory (CMT) to discuss the FOM, sensitivity S , and spectral responses in a plasmonic slot waveguide with a multimode stub resonator. Interestingly, single plasmonic induced transparency (PIT) or double PIT windows with Fano resonances are observed when we choose the proper width a and depth b . Meanwhile, the depth b , width a , and thickness h have significant influence on spectra, sensitivity S , and FOM in our proposed structure. More importantly, the FOM and sensitivity S in this single multimode stub resonator are superior to those in multistub/cavity MDM waveguide systems [20,23,24]. In addition, the single multimode stub resonator also has the advantages of easy fabrication and compactness.

Figure 1 shows a MDM waveguide with a stub resonator. The dielectric and metal in the structure are air and silver, respectively. $h = 1500$ nm is the thickness of the silver, $w = 50$ nm is the width of the bus waveguide, and b and a are the depth and width of the stub resonator, respectively. The permittivity of silver is described by the Drude model, $\epsilon(\omega) = 3.7 - \omega_p^2/(\omega^2 + i\omega\gamma_p)$, with $\omega_p = 1.38 \times 10^{16}$ rad/s and $\gamma_p = 2.73 \times 10^{13}$ rad/s [25]. When a plane wave is injected and coupled into the bus waveguide, an SPP wave forms on the metallic interfaces and is confined in the waveguide. To calculate transmission ($T = P_{\text{out}}/P_{\text{in}}$), the power monitors of P_{out} and P_{in} are placed at the locations in Fig. 1(b) [17]. The characteristic spectral responses of the structures are found through the three-dimensional (3D) finite-difference time-domain (FDTD) method [26]. The spatial and temporal steps are set as $\Delta x = \Delta y = \Delta z = 4$ nm and $t = \Delta x/2c$ (c is the velocity of light in vacuum). We perform the FDTD simulations with a perfect matched layer (PML) boundary condition at the x , y , and z directions.

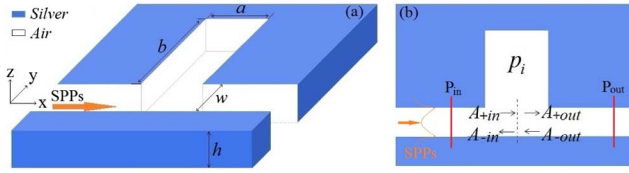


Fig. 1. (a) Schematic of an MDM slot waveguide side-coupled with a stub resonator. (b) CMT model for our proposed structure.

Although based on CMT analysis [17,20,27], our method is different from CMT in recent Letters. The previous Letter introduced CMT to describe indirect coupling among modes [27]. However, in our Letter, we demonstrate the direct coupling among modes through CMT. The multimode stub resonator, which has N modes, has a feature of direct coupling between arbitrary two modes. The CMT in this multimode stub can be described by a harmonic oscillator model as follows:

$$\begin{bmatrix} D_1 & j\mu_{12} & \cdots & j\mu_{1(N-1)} & j\mu_{1N} \\ j\mu_{21} & D_2 & j\mu_{23} & \cdots & j\mu_{2N} \\ \vdots & j\mu_{i2} & \ddots & j\mu_{i(N-1)} & \vdots \\ j\mu_{(N-1)1} & \cdots & j\mu_{(N-1)(N-2)} & D_{N-1} & j\mu_{(N-1)N} \\ j\mu_{N1} & j\mu_{N2} & \cdots & j\mu_{N(N-1)} & D_N \end{bmatrix} \cdot \begin{bmatrix} p_1 \\ \vdots \\ p_i \\ \vdots \\ p_N \end{bmatrix} = \begin{bmatrix} S_{+in} \sqrt{1/\tau_{w1}} \\ \vdots \\ S_{+in} \sqrt{1/\tau_{wi}} \\ \vdots \\ S_{+in} \sqrt{1/\tau_{wN}} \end{bmatrix}, \quad (1)$$

where $D_i = j\omega - j\omega_i + 1/\tau_{wi} + 1/\tau_{ci}$, ω_i is the resonant frequency of the i th mode in the stub, and $1/\tau_{wi} = \omega_i/(2Q_{wi})$ is the decay rate due to energy escaping into the bus waveguide. $1/\tau_{ci} = \omega_i/(2Q_{ci})$ is the decay rate due to intrinsic loss of the i th mode in the stub. $\mu_{ji} = \omega_i/(2Q_{di})$ is the coupling coefficients between the j th and i th modes [17]; Q_{ci} , Q_{wi} , and Q_{di} are cavity quality factors related to intrinsic loss, waveguide coupling loss, and direct coupling, respectively. With the conservation of energy, we get

$$\begin{aligned} S_{+out} &= S_{+in} - \sum_{i=1}^n \left(\sqrt{1/\tau_{wi}} \cdot p_i \right) \\ S_{-in} &= S_{-out} - \sum_{i=1}^n \left(\sqrt{1/\tau_{wi}} \cdot p_i \right). \end{aligned} \quad (2)$$

Using boundary conditions of $S_{-out} = 0$ and Eq. (1), the transmission coefficient $T_N = |S_{+out}/S_{+in}|^2$, the reflection coefficient $R_N = |S_{-in}/S_{+in}|^2$, and the absorption coefficient $A_N = 1 - T_N - R_N$. Thus, the transmission and reflection coefficients when $N = 1$ can be seen as follows:

$$T_1 = \left| 1 - \frac{1}{D_1 \tau_{w1}} \right|^2 \quad R_1 = \left| -\frac{1}{D_1 \tau_{w1}} \right|^2. \quad (3)$$

When there are two or three modes in the stub resonator, the transmission and reflection coefficients T_2 , T_3 , R_2 , and R_3 can be seen in the following form:

$$T_2 = \left| 1 - \frac{1}{D_1 \tau_{w1}} + \frac{\alpha_1 \delta_1}{\beta_1} \right|^2 \quad R_2 = \left| -\frac{1}{D_1 \tau_{w1}} + \frac{\alpha_1 \delta_1}{\beta_1} \right|^2, \quad (4)$$

$$T_3 = \left| 1 - \frac{1}{D_1 \tau_{w1}} + \frac{\alpha_1 \delta_1}{\beta_1} - \frac{\alpha_1 \chi_1 - \beta_1 \alpha_2}{\chi_1 \chi_2 - \beta_1 \beta_2} \left(\frac{\chi_2 \delta_1}{\beta_1} - \delta_2 \right) \right|^2, \quad (5a)$$

$$R_3 = \left| -\frac{1}{D_1 \tau_{w1}} + \frac{\alpha_1 \delta_1}{\beta_1} - \frac{\alpha_1 \chi_1 - \beta_1 \alpha_2}{\chi_1 \chi_2 - \beta_1 \beta_2} \left(\frac{\chi_2 \delta_1}{\beta_1} - \delta_2 \right) \right|^2, \quad (5b)$$

where

$$\alpha_1 = \frac{j\mu_{12} \sqrt{1/\tau_{w1}}}{D_1} - \sqrt{1/\tau_{w2}} \quad \alpha_2 = \frac{j\mu_{13} \sqrt{1/\tau_{w1}}}{D_1} - \sqrt{1/\tau_{w3}}, \quad (6)$$

$$\beta_1 = \frac{\mu_{12} \mu_{21}}{D_1} + D_2 \quad \beta_2 = \frac{\mu_{13} \mu_{31}}{D_1} + D_3, \quad (7)$$

$$\chi_1 = \frac{\mu_{21} \mu_{13}}{D_1} + j\mu_{23} \quad \chi_2 = \frac{\mu_{12} \mu_{31}}{D_1} + j\mu_{32}, \quad (8)$$

$$\delta_1 = \sqrt{1/\tau_{w2}} - \frac{j\mu_{21} \sqrt{1/\tau_{w1}}}{D_1} \quad \delta_2 = \sqrt{1/\tau_{w3}} - \frac{j\mu_{31} \sqrt{1/\tau_{w1}}}{D_1}. \quad (9)$$

For numerical understanding of Eqs. (3)–(5), the FDTD simulation is provided for structure when $h = 1500$ nm, $a = 300$ nm, $b = 325$ nm, 450 nm, and 485 nm, respectively. In Fig. 2, the red (black) solid line is the transmission (reflection) spectra calculated by FDTD, and the red (black) circle marked line is the transmission (reflection) spectra calculated by CMT. In order to illustrate the phenomenon in Fig. 2(a), the magnetic field H_z is depicted in Figs. 2(c)–2(h). The transmission spectrum shows a dip when $b = 325$ nm. Equation (3) can describe the transmission and reflection spectra when there

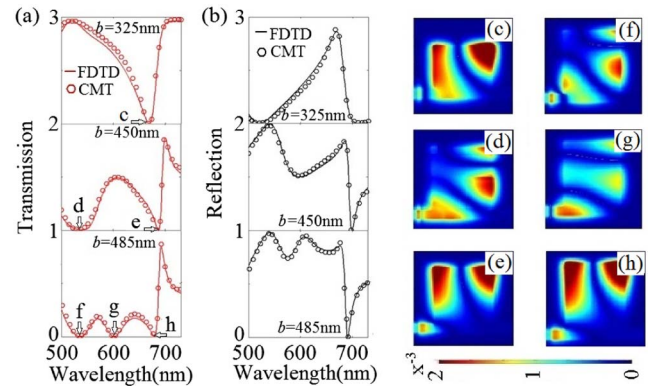


Fig. 2. (a) and (b) Transmission and reflection spectra with $a = 300$ nm and $h = 1500$ nm, yet with the depth $b = 325$, 450, and 485 nm. (c)–(h) Magnetic field H_z for different depth b at various wavelengths.

is only one mode in the stub. It is obvious that single PIT as well as Fano resonance has occurred in Fig. 2(a) when $b = 450$ nm. The PIT can be seen as the symmetrical case of the Fano resonance. We can introduce Eq. (4) to analyze the transmission and reflection spectra when there is a coupling between TM_{11} and TM_{10} in the stub. When the depth $b = 485$ nm, the double PIT and the Fano resonance are observed in Fig. 2(a). Equation (5) can describe the optical properties when there are three modes in the single stub. Observing from Fig. 2, we can find the CMT results are in good agreement with the FDTD results. In addition, we can find the stub can support more modes with an increase of the depth b . This theory model can effectively describe the transmission and reflection spectra and provide guidance for the multimode resonator.

Based on the above study, we investigate FOM and sensitivity in this single multimode stub system. We introduce the definition of the $FOM = \Delta I / (\Delta n \cdot I) = [T(\omega, n_0 + \Delta n) - T(\omega, n_0)] / [\Delta n \cdot T(\omega, n_0)]$ [20], $FOM^* = \max[FOM]$, where $T(\omega, n_0)$, $T(\omega, n_0 + \Delta n)$ are transmissions at frequency ω for the stub with dielectric material refractive indices n_0 and $n_0 + \Delta n$, respectively. Here, we also introduce the definition of sensitivity $S = \Delta T / \Delta n = [(T(\omega, n_0 + \Delta n) - T(\omega, n_0)) / \Delta n]$. The maximum of ΔT is 1; when $\Delta n = 0.01$, the maximum of S is 100. So as compared with FOM and sensitivity S in recent Letters [20,23,24], we investigate the FOM when n increases. Figure 3(a) shows transmission spectra when the refractive index n in the stub resonator increases from 1.00 to 1.03 with $a = 300$ nm, $b = 485$ nm, and $h = 1500$ nm. We can find that the transmission spectra shift to longer wavelengths and almost keep the same lineshape. The transmission spectra and FOM when $\Delta n = 0.01$, $a = 300$ nm, $b = 485$ nm, and $h = 1500$ nm are shown in Fig. 3(b). FOM^* nearly appears at the transmission dips, which can be explained by the lowest initial intensity T here. Three FOM peaks are observed in Fig. 3(b). A FOM^* of $\sim 23,100$ at 678 nm is obtained. Then the sensitivity S is discussed when $\Delta n = 0.01$, $a = 300$ nm, $b = 485$ nm, and $h = 1500$ nm as shown in Fig. 3(c). We can find that sensitivity S at peak 2 and peak 3 first increases and then decreases. The sensitivity S at peak 1 increases gradually as b increases. The sensitivity S at peak 3 can reach to 75.7. In order to discuss the FOM^* in detail, we numerically and theoretically investigate FOM^* with $a = 300$ nm, $b = 485$ nm, and $h = 1500$ nm

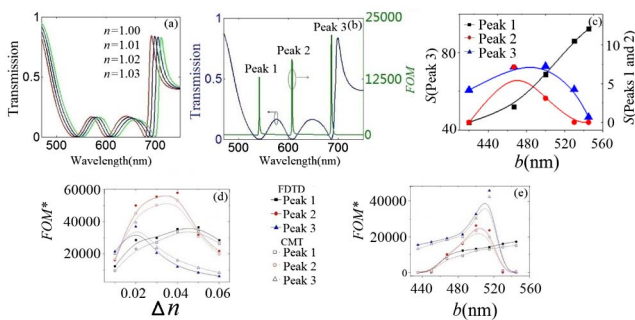


Fig. 3. (a) Transmission spectra when n increases from 1.00 to 1.03, with $a = 300$ nm, $b = 485$ nm, and $h = 1500$ nm. (b) Transmission spectra when $a = 300$ nm, $b = 485$ nm, and $h = 1500$ nm and FOM with $\Delta n = 0.01$. (c) Sensitivity S as a function of b . (d) FOM^* as a function of Δn . (e) FOM^* as a function of b .

when Δn increases from 0.01 to 0.06 in Fig. 3(d). The solid marked line is the FDTD results, and the hollow marked line is the CMT results. We can find that FOM^* at peak 1, peak 2, and peak 3 first increases and then decreases. The FOM^* at peak 2 can reach to 59,010 when $\Delta n = 0.04$, which is much higher than that in [20–24]. At last, we discuss FOM^* as a function of b , with $\Delta n = 0.01$, yet with $a = 300$ nm and $h = 1500$ nm. We can see the trend of FOM^* is the same as that of sensitivity S at peaks 1, 2, and 3. Observing from Figs. 3(d) and 3(e), we can find the CMT results are in accord with the FDTD results. These results may provide guidance for fundamental research of the integrated plasmonic nanosensor applications.

The width a , which has an important influence on the optical properties, sensitivity S and FOM, is studied in this section. Figure 4(a) shows the transmission spectra with the same parameters $b = 485$ nm and $h = 1500$ nm, yet with the width $a = 275$ nm, 300 nm, 325 nm, and 350 nm, respectively. We can see single PIT when $a = 275$ nm, and double PIT windows with $a = 300$ nm. As the width a continues to increase, the PIT window gradually disappears. Then we discuss the FOM^* as a function of the width a at the peaks 1, 2, and 3 through both FDTD simulations and CMT. With the increasing of the width a , we can see the FOM^* at peak 1 decreases. And the FOM^* at peak 2 and peak 3 first increases and then decreases as the width a increases. It is interesting that the FOM^* at peak 3 can reach to 34,300. Figure 4(c) shows the sensitivity S as a function of a when $\Delta n = 0.01$. We can see the sensitivity S at peak 1 decreases with the increasing of a , and the sensitivity S at peak 2 and peak 3 first increases and then decreases. The value of sensitivity S at peak 3 is much higher than that at peak 1 and peak 2. These results may play a guiding role for plasmonic nanosensor applications.

At last, we investigate the transmission (T), reflection (R), and absorption (A) spectra with the same parameters $a = 300$ nm and $b = 485$ nm, yet with the thickness $h = 1500$ nm, 1000 nm, and 500 nm, respectively. It is interesting that the transmission shows double PIT and Fano resonances and decreases as h ranges from 1500 to 500 nm as shown in Figs. 5(a)–5(c). At the same time, the reflection also decreases with the decreasing of the thickness h . The increasing

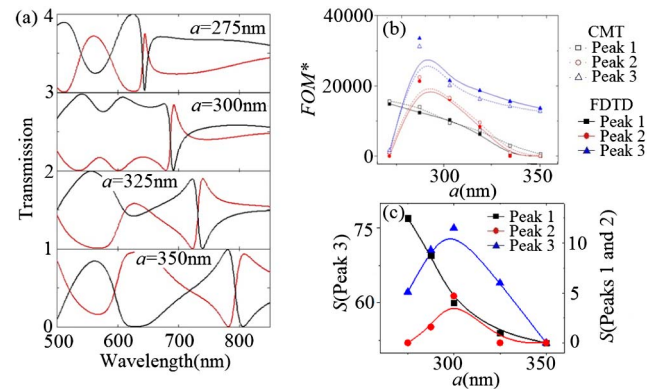


Fig. 4. (a) Transmission and reflection spectra with $b = 485$ nm and $h = 1500$ nm, yet with $a = 275$ nm, 300 nm, 325 nm, and 350 nm, respectively. (b) FOM^* as a function of a with $\Delta n = 0.01$, $b = 485$ nm, and $h = 1500$ nm. (c) Sensitivity S as a function of a .

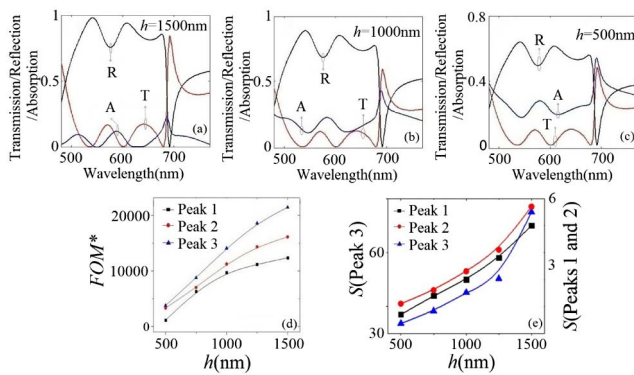


Fig. 5. (a)–(c) Transmission (T), reflection (R), and absorption (A) spectra with $a = 300$ nm and $b = 485$ nm, yet with $h = 1000$ nm, 750 nm, and 500 nm, respectively. (d) FOM^* as a function of h with $\Delta n = 0.01$, $a = 300$ nm, and $b = 485$ nm. (e) Sensitivity S as a function of h with $\Delta n = 0.01$, $a = 300$ nm, and $b = 485$ nm.

of the absorption is a reason for this phenomenon. In other word, the small size in the z direction cannot hold the whole z -component of input light, so part of the power is absorbed by the PMLs. Then we investigate the FOM^* as a function of the thickness h . In Fig. 5(d), we can find that the FOM^* increases with the increasing of the thickness h . At last, we discuss the sensitivity S as a function of h in Fig. 5(e). We can see the sensitivity S increases at peak 1, peak 2, and peak 3 with the increasing of h . These results may provide guidance for tuning the plasmonic nanosensor in our proposed structures.

According to the results of the preceding research, we find our proposed structure could be used for gas sensing. The FOM^* can reach up to 59,010 and the maximum of the sensitivity S is as high as 75.7. The previous Letter demonstrated the nanoplasmonic structure with FOM^* of 22,000, and its maximum of the sensitivity S is 60 through FDTD simulations [20,24]. Thus, our proposed single multimode stub is superior to the other gas sensors.

From a practical point view, the silver material will be oxidized in air. Through our numerical simulations, we can find the oxidation layer has an obvious effect on transmittance, FOM , and sensitivity S . The oxidation layer makes the sensing performance of the gas sensor no longer as good as before. Thus, avoiding oxidization as well as keeping the outstanding performance of the device will be a meaningful research. There may be some experimental methods to avoid the oxidization, such as making the surface of the silver passivated. We hope our numerical simulations may provide guidance for experiment research.

In summary, we have numerically and theoretically investigated spectral responses and sensing performance in a MDM waveguide side-coupled with a multimode stub resonator. Single PIT or double PIT as well as Fano resonances are observed in our Letter. The CMT results are in good agreement

with the FDTD simulations. Through adjusting the parameters of the stub resonator, the ultrahigh FOM is realized in a single stub waveguide system. Owing to the simple configuration and compactness, the ultracompact structure holds great potential in highly integrated optical circuits.

Funding. National Natural Science Foundation of China (NSFC) (61275174); Central South University (CSU) (2016zzts017).

REFERENCES

1. D. Gramotnev and S. Bozhevolnyi, Nat. Photonics **4**, 83 (2010).
2. E. N. Economou, Phys. Rev. **182**, 539 (1969).
3. J. Park, K. Kim, I. Lee, H. Na, S. Lee, and B. Lee, Opt. Express **18**, 598 (2010).
4. I. Zand, M. Abrishamian, and T. Pakizeh, IEEE J. Sel. Top. Quantum Electron. **19**, 4600505 (2013).
5. H. Wang, J. Yang, J. Zhang, J. Huang, W. Wu, D. Chen, and G. Xiao, Opt. Lett. **41**, 1233 (2016).
6. J. Yang, J. Lee, J. Kang, S. J. Oh, H. J. Ko, J. H. Son, K. Lee, J. S. Suh, Y. M. Huh, and S. Haam, Adv. Mater. **21**, 4339 (2009).
7. Z. He, H. Li, S. Zhan, B. Li, Z. Chen, and H. Xu, Sci. Rep. **5**, 15837 (2015).
8. J. Chen, Z. Li, X. Zhang, J. Xiao, and Q. Gong, Sci. Rep. **3**, 1451 (2013).
9. E. Bévilacqua, J. Colombier, V. Recoules, H. Zhang, C. Li, and R. Stoian, Phys. Rev. B **93**, 165416 (2016).
10. M. Hashemi, M. H. Farzad, N. A. Mortensen, and S. Xiao, J. Opt. **15**, 055003 (2013).
11. H. Lu, B. P. Cumming, and M. Gu, Opt. Lett. **40**, 3647 (2015).
12. C. Min and G. Veronis, Opt. Express **17**, 10757 (2009).
13. Y. Huang, C. Min, and G. Veronis, Opt. Express **20**, 22233 (2012).
14. D. Pile, T. Ogawa, D. Gramotnev, Y. Matsuzaki, K. Vernon, K. Yamaguchi, T. Okamoto, M. Haraguchi, and M. Fukui, Appl. Phys. Lett. **87**, 261114 (2005).
15. Y. Huang, G. Veronis, and C. Min, Opt. Express **23**, 29882 (2015).
16. Z. He, H. Li, S. Zhan, G. Cao, and B. Li, Opt. Lett. **39**, 5543 (2014).
17. G. Cao, H. Li, S. Zhan, Z. He, Z. Guo, X. Xu, and H. Yang, Opt. Lett. **39**, 216 (2014).
18. H. Lu, X. Liu, D. Mao, Y. Gong, and G. Wang, Opt. Lett. **36**, 3233 (2011).
19. Z. Chen, H. Li, S. Zhan, B. Li, Z. He, H. Xu, and M. Zheng, Sci. Rep. **6**, 24446 (2016).
20. S. Zhan, H. Li, Z. He, B. Li, Z. Chen, and H. Xu, Opt. Express **23**, 20313 (2015).
21. Y. Huang, C. Min, P. Dastmalchi, and G. Veronis, Opt. Express **23**, 14922 (2015).
22. Z. He, Y. Peng, B. Li, Z. Chen, H. Xu, M. Zheng, and H. Li, Appl. Phys. Express **9**, 072002 (2016).
23. H. Lu, X. Liu, D. Mao, and G. Wang, Opt. Lett. **37**, 3780 (2012).
24. J. Chen, Z. Li, Y. Zou, Z. Deng, J. Xiao, and Q. Gong, Plasmonics **8**, 1627 (2013).
25. E. D. Palik, Handbook of Optical Constants in Solids (Academic, 1982).
26. A. Taflov and S. Hagness, Computational Electrodynamics: The Finite-Difference Time-Domain Method, 3rd ed. (Artech House, 2005).
27. H. Lu, X. Liu, and D. Mao, Phys. Rev. A **85**, 053803 (2012).